Influence of nanosecond laser surface patterning on dental 3Y-TZP: Effects on the topography, hydrothermal degradation and cell response

N. Garcia-de-Albeniz [a,b], M.-P. Ginebra [b,c,d], E. Jimenez-Piqué [a,c], J.J. Roa [a,c,*], C. Mas-Moruno [b,c,**]

[a] Center for Structural Integrity, Reliability and Micromechanics of Materials (CIEFMA), Department of Materials Science and Engineering, Universitat Politècnica de Catalunya-BarcelonaTECH, 08019 Barcelona, Spain
[b] Biomaterials, Biomechanics and Tissue Engineering Group (BBT), Department of Materials Science and Engineering, Universitat Politècnica de Catalunya, BarcelonaTECH, 08019 Barcelona, Spain
[c] Barcelona Research Center in ssMultiscale Science and Engineering, Universitat Politècnica de Catalunya-BarcelonaTECH, 08019 Barcelona, Spain
[d] Institute for Bioengineering of Catalonia (IBEC), Barcelona Institute of Science and Technology, 08028 Barcelona, Spain

ARTICLE INFO

ABSTRACT

Objectives: Laser surface micropatterning of dental-grade zirconia (3Y-TZP) was explored with the objective of providing defined linear patterns capable of guiding bone-cell response.
Methods: A nanosecond (ns-) laser was employed to fabricate microgrooves on the surface of 3Y-TZP discs, yielding three different groove periodicities (i.e., 30, 50 and 100 μm). The resulting topography and surface damage were characterized by confocal laser scanning microscopy (CLSM) and scanning electron microscopy (SEM). X-Ray diffraction (XRD) and Raman spectroscopy techniques were employed to assess the hydrothermal degradation resistance of the modified topographies. Preliminary biological studies were conducted to evaluate adhesion (6 h) of human mesenchymal stem cells (hMSC) to the patterns in terms of cell number and morphology. Finally, *Staphylococcus aureus* adhesion (4 h) to the microgrooves was investigated.
Results: The surface analysis showed grooves of approximately 1.8 μm height that exhibited surface damage in the form of pile-up at the edge of the microgrooves, microcracks and cavities. Accelerated aging tests revealed a slight decrease of the hydrothermal degradation resistance after laser patterning, and the Raman mapping showed the presence of monoclinic phase heterogeneously distributed along the patterned surfaces. An increase of the hMSC area was identified on all the microgrooved surfaces, although only the 50 μm periodicity, which is closer to the cell size, significantly favored cell elongation and alignment along the grooves. A decrease in *Staphylococcus aureus* adhesion was observed on the investigated micropatterns.
Significance: The study suggests that linear microgrooves of 50 μm periodicity may help in promoting hMSC adhesion and alignment, while reducing bacterial cell attachment.

1. Introduction

Over the last decades, the field of dentistry is increasingly shifting toward metal-free tooth-colored dental implants in order to avoid allergic reactions [1–3] and aesthetic concerns [4,5] associated to traditional titanium components. At present, Tetragonal Zirconia Polycrystal stabilized with 3% molar yttrium oxide (also denoted as 3Y-TZP) is by far the most commonly demanded dental substitute because of the combination of adequate mechanical properties (fracture toughness, strength, and hardness), high corrosion resistance and superior aesthetic appearance [6–8]. Additionally, 3Y-TZP exhibits excellent biocompatibility [9,10] and it has been demonstrated to be less prone to bacterial plaque accumulation and peri-implantitis in comparison to titanium [11–14], thus making this bioceramic material very attractive for dental applications.

The success of dental implants, which are surgically inserted into the

---

jawbone, is largely determined by the osseointegration process. It is essential to achieve a direct and strong contact between the implant and the surrounding bone to ensure an optimal mechanical stability and long-term durability of the implant [15].

The selection of the material and the surface characteristics of the implant are crucial factors that influence the initial stages following implantation and may ultimately determine the implant's success. This can be a disadvantage for zirconia given that it is a relatively inert material. Furthermore, although promising short-term survival rates have been reported for 3Y-TZP are positive, there is limited long-term survival data available on the performance and longevity of zirconia implants [16–18].

Given that the implant surface is key to modulate the initial steps of the osseointegration [19], surface modification of 3Y-TZP dental implants is a well-stablished approach aimed at improving the biological response of this materials [20,21]. The chemical composition, wettability, and roughness of the implant surface affect a wide range of cellular activities that are crucial in the osseointegration process, including: adhesion, spreading, morphology, proliferation, and differentiation of mesenchymal stem cells (MSC) [22–24].

This article particularly focuses on how micro/nanotextured 3Y-TZP influences the early response of hMSCs in terms of adhesion and cell morphology. Cell adhesion is crucial in the initial steps of osseointegration. It is well known that increasing surface roughness improved hMSCs adhesion and spreading by increasing the available surface area to interact with and by providing these cell more contact points to anchor to [25,26]. Within this respect, according to Albrektsson and Wennerberg a surface with a moderate average surface roughness (S_a) between 1 and 2 μm showed the stronger bone response than smoother or rougher ones [27]. Also, the morphology of these cells influences their ability to form stable attachments, which is critical for the subsequent stages of osseointegration. On this respect, the topography of the substrate can guide and influence the cell's shape. It has been proven that providing the surface with additional texture, such as groove-like structures, can activate specific signaling pathways, leading to cytoskeletal reorganization and changes in the cell morphology, and subsequently stimulate cell contact guidance, i.e. cell alignment, differentiation and migration [28–32].

Nevertheless, the osseointegration can be disbalanced by the bacteria colonizing the implant surface. In fact, the fate of the implant is dictated by a process known as "race for the surface", with is a competition between the tissue integration vs. the microbial adhesion and biofilm growth [33]. As for the host tissue cells, bacterial adhesion is also influenced by the topographical properties of the substrate [34,35]. Depending on the surface structural features the effect on bacterial attachment can be either deterrent or attractive [36]. The latter is critical and must be avoided, since it could lead to a destructive inflammatory process called peri-implantitis [37].

Several topographical modification strategies have been explored to improve cell response on 3Y-TZP surfaces [21], including grinding [38–40], sandblasting [41–43], chemical etching [44–47] and laser treatment [31,48–52]. Of particular interest is the laser patterning technique, since it aims at designing detailed, accurate and periodic topographies able to target specific cell functions, and not merely increasing the surface roughness. Within this context, different structures have been already patterned on zirconia (e.g. grooves [31,53–56], pits [57] and grids [54,58]), which have demonstrated to promote particular cell functions (e.g. proliferation, differentiation and migration) that may be beneficial for a faster and better bone-implant interlocking. Moreover, 3Y-TZP surfaces have been patterned with different laser types (pulse duration and wavelength), and a wide variety of processing parameters, thus leading to a large variability on the achieved structures [50]. Nevertheless, the information available in this field is scarce and not yet enough to understand precisely the impact of the topographical features (i.e. pattern type, periodicity or depth) on cell functions and bacterial adhesion.

Another important aspect to take into consideration is that 3Y-TZP is very sensitive to any surface alteration given its brittle nature. As a matter of fact, laser surface modification is accompanied by superficial and microstructural defects, which can negatively affect the mechanical properties of 3Y-TZP [52,59,60]. Besides, one major concern with 3Y-TZP is the hydrothermal degradation (also known as ageing or low-temperature degradation – LTD) that the material suffers when in contact with water or exposed to a humid environment [61]. This degradation mechanism leads to microcracking and grain pull-out, which, from a clinical point of view, can be detrimental for the long-term integrity of the implant [52,62–65]. Moreover, the laser type employed and the processing parameters affect both the mechanical properties and LTD of 3Y-TZP. In the particular case of nanosecond (ns-) laser, the regime selected for this study, the material is mainly removed by a thermal mechanism rather than by ablation. Consequently, thermal damage in the form of material melting, microcracks, and micropores, together with the introduction of residual stresses, can be critical for the stability of the material [64,66]. Therefore, it is of vital importance to carefully optimize the laser processing parameters in order to minimize the thermal damage.

The studies currently available in the literature tend to either focus on the characterization of the physicochemical, mechanical or LTD changes of 3Y-TZP after the laser patterning, or evaluate the improvement on the cell response induced by the patterns. However, both aspects, which are very relevant to each other, are seldom investigated together. Moreover, the exact characteristics of the optimal laser patterns that provide the best cell responses still remain unclear.

In the present work ns-laser surface micropatterning of dental-grade 3Y-TZP was explored with the objective of providing a groove-like topography able to guide bone-cell response. The influence of the processing parameters on the quality and definition of the patterns were evaluated in terms of pattern depth and pile-up, allowing us to select the optimal processing parameters to produce microgrooves on 3Y-TZP with different periodicity i.e. above, below or in the range of cell size. The surface damage and the changes in the LTD resistance generated during the surface modification were subsequently evaluated, as well as the hMSCs adhesion and morphology as a function of the pattern periodicity. Finally, *Staphylococcus aureus* (S. aureus) bacterial adhesion to the microgrooves was also investigated.

2. Materials and methods

2.1. Material processing

Commercially available 3Y-TZP powder stabilized with 3 mol% yttria (TZ-3YSB-E, Tosoh) was used to produce 15 mm diameter disc-shaped specimens. The samples were shaped by cold isostatic pressing at 288 MPa and next the green bodies were sintered in air at 1450ºC for 2 h with constant heating and cooling rates of 6 °C/min. Subsequently, the surfaces of the discs were grounded and mirror-like polished by using diamond suspensions of decreasing particle size (30–6–3 μm), and a finalizing polishing step with alumina of 0.02 μm particle size.

2.2. Laser patterning

The surface patterning was carried out using the Spectra-Physics Explorer One 349–120 laser source operating at 349 nm wavelength, < 5 ns pulse duration, and 120 μJ energy per pulse. A Design of Experiments (DoE) was planned to study the influence of the key laser parameters (intensity, scan speed and frequency) on the morphology of the patterns, which has been included as supplementary material (S1). The topographies produced were characterized via Atomic Force Microscopy (AFM, Dimension 3100 from Bruker) and Laser Scanning Confocal microscopy (LSCM, Olympus Lext OLS3100). After this process of optimization, the laser parameters selected were: a laser intensity of 2.5 A, 500 Hz output frequency, and 2 bit/ms scan speed. All the samples

were treated with a single pulse.

Subsequently, three different topographies were engraved on the 3Y-TZP discs, consisting on parallel grooves with different periodicity. In detail, 30, 50 and 100 μm periodicities were produced and mirror-like polished 3Y-TZP was included as a control. The specimens and labels used during this work are summarized in Table 1.

2.3. Surface characterization

Scanning Electron Microscopy (SEM, JEOL JSM-7001 F) was used to visualize the topography of the laser-treated samples and to identify the surface damage associated to the treatment. LSCM was used to obtain the surface profiles of the three patterns and to measure the characteristics of those profiles (i.e. *groove width and height*). To this end, images of 96 × 128 μm were taken with 50x magnification. Two specimens of each condition were used and 9 images per sample were taken for statistical significance.

2.4. Hydrothermal degradation

Accelerated degradation tests were performed in water steam at 134 °C and 2 bars of pressure (Micro8, Selecta) to evaluate the hydrothermal degradation resistance of the samples after the laser treatment. The samples were degraded for 10 h, which is equivalent to 30–40 years when implanted in the body [62].

X-Ray Diffraction (XRD) was used to evaluate the crystalline phases of the specimens before (before HD) and after (HD10h) the hydrothermal degradation. XRD spectra were recorded on a diffractometer (D8-Advance, Bruker) using Cu Kα radiation (40 kV and 30 mA) in an angle range of $20° \leq 2\theta \leq 70°$ at a scan rate of 1 s/step and a scan size of $0.02°$. The monoclinic (m-) volume fraction (V_m) was estimated by the equation proposed by Toraya *et al.* [67] as follows:

$$V_m = \frac{1.311\left[Im(\overline{1}11) + Im(111)\right]}{1.311\left[Im(\overline{1}11) + Im(111)\right] + It(101)} \quad (1)$$

where I_m and I_t correspond to the intensities of the monoclinic (m-) and tetragonal (t-) peaks, respectively.

Confocal Raman Spectroscopy (Cm-RS, inVia Qontor, Renishaw) technique was used to analyze the m-phase distribution along the patterns. A 532 nm wavelength laser was used as a source of excitation and 1 s spectrum integration time. An area of 30 × 50 μm was selected for the analysis and the V_m was calculated by the equation proposed by Katagiri *et al.* [68]:

$$V_m = \frac{I_m^{181} + I_m^{190}}{2.2\left(I_t^{247}\right) + I_m^{181} + I_m^{190}} \quad (2)$$

where I_m and I_t correspond to the integrated intensities of the m- and t-bands, respectively.

Both XRD and Raman spectroscopy analyses were performed using one sample per condition.

2.5. Biological characterization

2.5.1. Cell culture

Human mesenchymal stem cells (hMSCs) at passage five were cultured in Advanced Dulbecco's Modified Eagle's Medium (DMEM) supplemented with 10% (v/v) fetal bovine serum (FBS), 50 U/mL penicillin, 50 U/mL streptomycin and 1% (w/v) L-glutamine and maintained at 37ºC in a humidified 5% CO_2 atmosphere. The culture medium was changed every 3–4 days until a confluence of 90% was reached. At that point, the hMSCs were ready for the assay and were detached using trypsin-EDTA.

2.5.2. Cell adhesion and immunofluorescence analysis

An immunofluorescence analysis was performed in order to evaluate the effect of the laser patterns on cell attachment and morphology. First, the 3Y-TZP samples were sterilized with 70% (v/v) ethanol during 15 min, rinsed thrice with phosphate-buffered saline (PBS), and transferred to a 24-well plate to carry out the experiment. Subsequently, hMSCs at passage 6 were seeded on the 3Y-TZP samples at a concentration of 5000 cells/well in serum-free culture medium. After 6 h of incubation, the medium was aspirated and the wells washed with PBS to eliminate non-adherent cells. Finally, adherent cells were fixed using paraformaldehyde (PFA, 4% w/v in PBS) during 30 min, washed again thrice with PBS and stored at 4ºC in PBS.

For morphology assessment via fluorescence staining, the cells were permeabilized with 0.05% (w/v) Triton X-100 in PBS for 20 min followed by a 30 min blocking step with bovine serum albumin (BSA, 1% (w/v) in PBS). The cytoskeletal actin filaments (F-actin) were stained using phalloidin (1:400, in triton 0.05%, 1 h). Focal adhesions (FAs) were stained with mouse anti-vinculin (1:400, in BSA 1%, 1 h) followed by Alexa488 goat antimouse IgG antibody ((2drops/Ml, in triton 0.05%, 1 h). The nuclei was stained with 4′,6-diamidino-2- phenylindole (DAPI) (1:1000, in PBS-glycine 20 mM) for 2 min. PBS-glycine was used in between all steps to rinse the samples (3 times x 5 min). Finally, the specimens were mounted in Mowiol 4–88, and examined by fluorescence LSCM (Carl Zeiss LSM 800). The 5x objective was employed to observe the cell adhesion (i.e. cell numbers), 10x magnification was used to examine cell area (i.e. cell spreading) and morphology, and 40x magnification for the FAs.

The experiment was performed using triplicates. The acquired images were analyzed using Fiji/ImageJ image processing package. Minitab software was used for the statistical analysis, in which the statistical differences ($p < 0.05$) among the conditions of the study were assessed by ANOVA using Tukey test and confirmed by Mann-Whitney nonparametric test.

Once all images were obtained, the samples were immersed in PBS at room temperature for 1–2 days, while gently shaking. The mounting medium was dissolved and the coverslips removed. Cells were then dehydrated through immersion in increasing concentrations of ethanol and visualized by Field Emission Scanning Electron Microscopy (FESEM, Carl Zeiss Neon 40).

2.5.3. Bacterial culture

For the bacterial adhesion study, *Staphylococcus aureus* (*S. aureus*) was selected as model of gram-positive bacteria. *S. aureus* was inoculated in 10 mL of sterilized Brain Heart Infusion Broth (BHI) (Difco) and incubated at 37ºC overnight in order to let bacteria grow.

2.5.4. Bacterial adhesion by live/dead assay

A live/dead assay was performed in order to evaluate the antimicrobial properties of the laser patterned 3Y-TZP. Before conducting the experiment, the 3Y-TZP samples were sterilized by immersing them in 70% ethanol during 15 min, washed trice with PBS and transferred into a 12-well plate. Meanwhile, the optical density of the bacteria from the incubated inoculum was measured at the wavelength of 600 nm and adjusted to 0.20 ± 0.01, which corresponds to a concentration of approximately 10^8 colony forming units (CFU)/mL. Next, the bacteria were diluted 1:5 times to a concentration of approximately 2×10^7 CFU/mL, seeded on the 3Y-TZP samples with 1 mL for each specimen, and incubated during 4 h at 37ºC. The assay was performed in static conditions and three replicas of each working condition were employed.

Table 1
Label and description of the specimens used in the study.

Label	Description
CTRL	Mirror-like polished 3Y-TZP samples used as reference.
L30	Laser patterned samples with a groove periodicity of 30 μm.
L50	Laser patterned samples with a groove periodicity of 50 μm.
L100	Laser patterned samples with a groove periodicity of 100 μm.

Once the incubation time was over, the non-adherent bacteria were removed by washing the samples trice with PBS. The adherent bacteria were fixed using glutaraldehyde (2.5% w/v in PBS) for 20 min, washed again thrice with PBS and stored at 4ºC in PBS. Then, the bacterial attachment and viability were analyzed using a LIVE/DEAD BackLight Bacterial Viability Kit (Thermo Fisher). All bacteria are stained by the SYTO 9 green-fluorescent nucleic acid staining agent, which penetrates both undamaged and damaged cell membranes, while dead bacteria are labeled by the red-fluorescent nucleic acid staining agent propidium iodide, which only penetrates damaged membranes. A solution containing 39 μL of the two dyes in 13 mL of PBS was prepared, and 1 mL of that solution was added to each sample and incubated at room temperature in the dark for 15 min. Subsequently, the samples were washed trice with PBS.

A fluorescence CLSM was used to acquire fluorescence images of the bacteria under the 63x magnification. Image J software was used to quantify the live bacteria from captured images by measuring the area of the green fluorescence. Then, the bacterial attachment to the microgrooves was analyzed by calculating the ratio of the live bacteria on each pattern (% area of green fluorescence) compared to the adhesion on the polished 3Y-TZP (CTRL).

Once all images were obtained, the samples were immersed in PBS at room temperature for 1–2 days, while gently shaking. The mounting medium was dissolved and the coverslips removed. The bacteria were then dehydrated through immersion in increasing concentrations of ethanol and visualized by Scanning Electron Microscopy.

3. Results

3.1. Topographical characterization

The SEM micrographs of microgroove patterns produced with the ns-laser are presented in Fig. 1. Three distinct linear patterns were generated by varying the periodicity between the grooves, with the objective of studying the influence of the periodicity on the cell behavior. In detail, these periodicities were chosen with respect to the dimension of hMSCs: 30 μm (below the cell size) (Fig. 1a), 50 μm (close to the cell size) (Fig. 1b) and 100 μm (above the cell size) (Fig. 1c).

The three structured patterns were composed of well-defined, reproducible and periodically spaced grooves, in which two distinctive areas could be differentiated (see Fig. 1c): the laser valley (light grey), and the non-treated zone (dark grey), which is reduced in size as the periodicity decreases. Table 2 summarizes the most relevant topographical characteristics of the patterns, which include: the periodicity (P), the total height of the grooves (H_t), the height (H_v) and width (W_v) of the laser valley, and the height (H_p) and width (W_p) of the pile-up. On the whole, only the periodicity varies among the three conditions. The other features were rather similar on the three patterns, since only the distance between the grooves varies but not the processing parameters

employed to texture the surfaces. Moreover, the ns-laser employed in the study led to the formation of pile-up structures at the sides of the grooves, because of the material melting, flowing and accumulation that occurred during the laser irradiation. From the measures presented on Table 2 it is evidenced that those topographical features appeared on the three patterns, independently on the periodicity. Also, the size of the pile-up was very pronounced when compared with the one of the grooves, given that the H_p and W_p are about a quarter and a third of the H_t and W_v, respectively.

Closer inspection of the microgrooves allowed to observe other topographical features and surface damage induced by the laser processing (see Fig. 2). Melting tracks appeared along the laser lines, indicating that the molten material flowed parallel to the grooves before it was resolidified and the pile-up was formed. Such topographical features provided the grooves with additional submicrometric size topography. Additionally, a network of interconnected microcracks was detected over the treated surface, as a result of the cracking of the resolidified material, and randomly distributed submicrometric size pits were observed in the surface. It should be mentioned that the extent and distribution of the generated surface damage was the same on the three patterns, given to the fact that none of the laser parameters changed, only the spacing between the grooves.

3.2. Microstructure

The XRD spectra of the microgrooved samples and the smooth CTRL condition are shown in Fig. 3a (CTRL, L30, L50 and L100). No peaks associated to the m-phase were detected in any of the laser-modified surfaces, indicating that the treatment did not induce $t{\to}m$ phase transformation. Indeed, the V_m calculated for the patterned 3Y-TZP samples was not significantly altered compared to CTRL, remaining below than 3% in all cases (see Fig. 3b): 1.43% (CTRL), 2.33% (L30), 2.06% (L50), and 1.87% (L100).

3.3. Low temperature degradation

Although the m-phase volume was found to be very low after the laser processing, the presence of the microcracks network on the laser tracks may affect the LTD resistance of 3Y-TZP. To characterize this, an accelerated aging test was performed for 10 h, which is proposed to simulate 30–40 years in vivo [62].

As depicted in Fig. 3a, the m-peaks $(-111)_m$, $(111)_m$ and $(002)_m$ appeared on all the aged zirconia samples (the CTRL and the patterned specimens), thus indicating that all the conditions suffered from LTD. Nevertheless, the m-phase volume calculated after ageing was different among the samples, as depicted in graph from Fig. 3b. The measured V_m *(%)* was, 31.92% in the CTRL, 43.64% in L30, 38.14% in L50, and 27.07% in L100 pattern. Accordingly, the long-term stability of 3Y-TZP was decreased on the 30 and 50 μm micropatterns when compared to

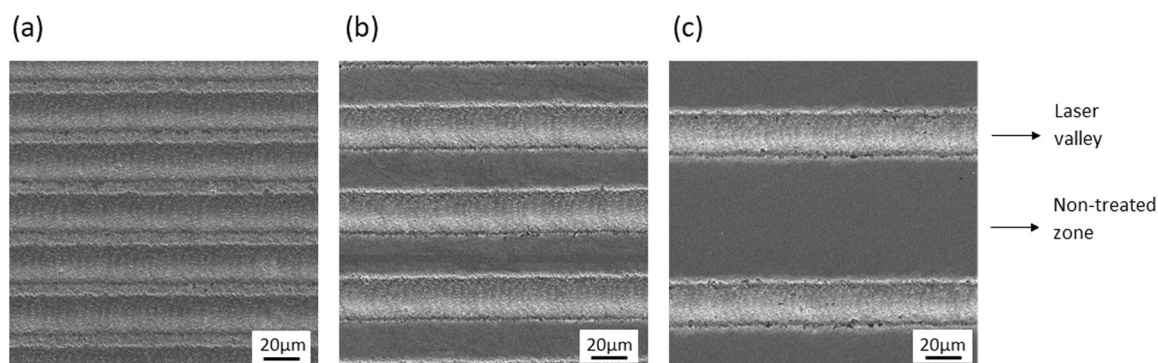**Fig. 1.** SEM micrographs of the microgroove pattern engraved on the 3Y-TZP disk as a function of the studied periodicities: (a) 30 μm, (b) 50 μm and (c) 100 μm.

Table 2

Topography analysis performed by the LCSM (50x). P is the periodicity; H_T, H_v, and H_p indicate the total height, the valley height, and the pile-up height (respectively); and W_v, W_p, indicate valley and pile-up width (respectively). All the measures are in μm.

Sample	P	H_T	H_v	H_p	W_v	W_p
L30	30.14 ± 0.57	1.76 ± 0.07	1.26 ± 0.08	0.43 ± 0.09	14.82 ± 0.45	4.39 ± 0.35
L50	50.29 ± 0.71	1.80 ± 0.08	1.30 ± 0.08	0.45 ± 0.04	14.71 ± 0.43	4.35 ± 0.29
L100	100.11 ± 0.54	1.82 ± 0.06	1.38 ± 0.07	0.45 ± 0.06	14.69 ± 0.36	4.48 ± 0.29
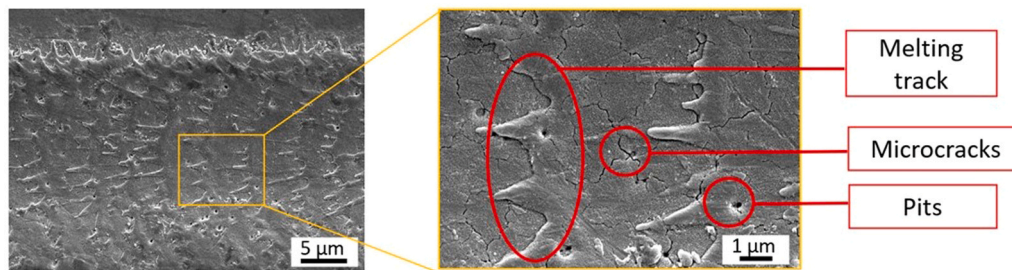
Fig. 2. SEM micrograph and magnification of the laser valley indicating the surface damage generated after the laser surface modification. The micrograph corresponds to the L50μm condition.
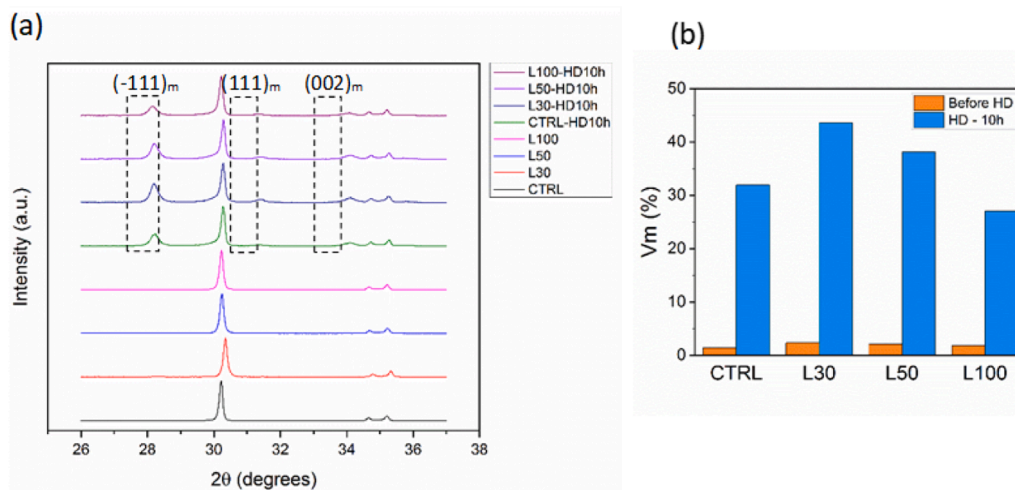
Fig. 3. (a) XRD analysis on the specimens before and after the LTD test and (b) quantification of the monoclinic volume fraction (*Vm*) of each condition before (orange) and after (blue) the LTD test.

the untreated condition, but it was slightly increased on the highest periodicity pattern (L100).

Additionally, Raman spectroscopy was performed on the aged samples to evaluate the distribution of the *m*-phase along the surface. As expected, the *m*-phase was homogeneously distributed on the polished 3Y-TZP (Fig. 4a), but, on the contrary, it was unevenly distributed along the surface of the three different patterns (Fig. 4b-d). On the laser structured 3Y-TZP, three zones could be differentiated according to the V_m measured (Fig. 4e): the flat part, the laser valley, and the pile-up zone. Among these regions, the maximum phase transformation is located at the pile-up zone. In contrast, the non-treated regions presented the lowest amount of *m*-phase, which was very similar to the CTRL.

3.4. Cell adhesion study

A cell adhesion assay was conducted to study the effect of the microgrooves on the adhesion and morphology of hMSCs (Fig. 5). The number of cells attached to CTRL and the patterned 3Y-TZP samples was found to be comparable, and although a trend towards higher cell attachment could be found for conditions L30 and L50, the differences were not statistically significant; thereby indicating that the number of adhering cells to the surfaces is not influenced by the engraved patterns, regardless of their periodicity (Fig. 5a). On the contrary, the area and morphology of the attached cells was clearly influenced by the microgrooves. In fact, the hMSCs adhered to the structured 3Y-TZP exhibited significantly ($p < 0.05$) bigger cell area (i.e. cell spreading) compared to the ones attached to the CTRL surface, yielding the highest values of spreading for condition L50 (Fig. 5b). Additionally, the cell aspect ratio was calculated as an indicator of the cell morphology and elongation: an aspect ratio close to 1 is related to rounded cells while higher values indicate that the cells have a more elongated shape. According to the results shown in Fig. 5c, the morphology of the cells depends on the groove periodicity. With more detail, the cells adhered to L30 and L100 samples displayed an aspect ratio close to 2, which was similar to the CTRL, indicating a rather circular morphology; in contrast the L50 pattern was able to promote a very elongated cell shape, with values of cell aspect ratio three times higher than the rest of conditions.

These findings are clearly evidenced in the fluorescence images presented in Figs. 5d to 5g. While the majority of the hMSCs attached to
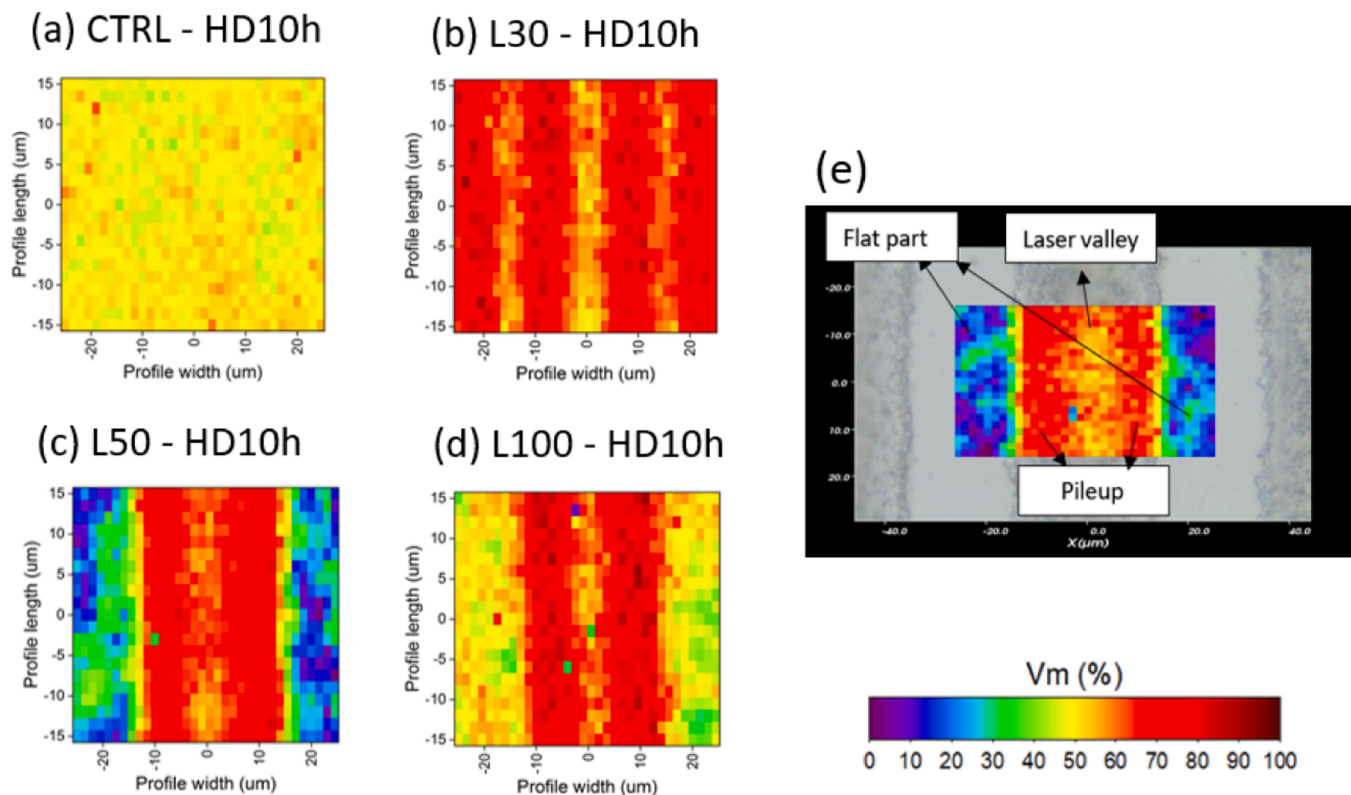
Fig. 4. Confocal micro-Raman spectroscopy analysis of the monoclinic (m-) phase distribution determined along the surface of the 10 h LTD samples: (a) CTRL, (b) L30, (c) L50 and (d) L100. (e) Image indicating the three spots that are distinguished on the L50 – HD10h sample according to the monoclinic volume fraction (V_m) measured.

polished zirconia surface presented a round morphology (Fig. 5**d**), very well spread and bigger cells were observed on the three microgroove patterns (Figs. 5**e** to 5**g**), indicating a notable enhancement in hMSC spreading. To further characterize the adhesion of hMSCs, the formation of FAs was evaluated via vinculin staining (Fig. S2, Supplementary Material). The cells adhering to the three laser-treated samples, but not to the control, presented nascent focal complexes, which are associated with a strong adhesion of the cell to the substrate.

Additionally, great changes in the cell-shape and alignment were observed only on the L50 condition. In this laser pattern, whose periodicity better mimic the dimension of the hMSCs, the cells acquired an elongated morphology and were clearly aligned according to the groove direction (see Fig. 5**f**). It is worth nothing that the elongated cells fitted mostly in between the laser grooves (on the non-treated zone), and not inside, as could be expected (Fig. 5**h**). Instead, the sub-microtopography generated inside of the grooves served as anchoring point for the cells, as evidenced in Fig. 5**i-j**, where filopodial extensions could be observed growing from the cell body to the lateral side of the laser structures. The other patterns displayed similar cell-groove interactions (Fig. S3b-**d**, Supplementary Material). On the contrary, round-shape and poorly spread cell were observed on the polished surface (Fig. S3a).

3.5. Bacterial adhesion

S. aureus was selected for this study, since it is one of the most common pathogens causing implant-related infections and a common cause of infections in many patients with dental implants [69,70]. The adhesion of this gram-positive bacteria was evaluated by live/dead staining after 4 h of incubation. Representative fluorescence images of the four samples are illustrated on Fig. 6, in which viable bacteria are stained green, while dead ones should be stained red. According to the images, the number of dead bacteria seems to be negligible on all the

samples, indicating that the microgroove topographies do not display a direct bactericidal effect on *S. aureus*. However, the analysis of the viable bacteria adhering to the samples revealed notable differences. In this regard, bacterial attachment on the CTRL specimens was found to be maximum (Fig. 6**a**). In contrast, a considerable reduction in the number of adherent *S. aureus* was observed on the 30 and 50 μm textured specimens (Figs. 6**b** to 6**d**).

To further characterize this observation, the percentages of the area covered by the live bacteria were calculated from the fluorescence images and are presented in Table 3. Bacterial adhesion on the laser-treated samples was compared to the untreated 3Y-TZP (CTRL), where the maximum value of bacterial attachment was achieved (100%). In comparison, the colonization area was significantly reduced in two of the patterns: the greatest decrease was achieved on the L30 pattern (22.5%), followed by the L50 condition (17.8%).

S. aureus adhesion was further characterized by SEM and the corresponding images have been included in the supplementary material (Fig. S4.**1**). In accordance with the fluorescence images, there is a decrease in the number of bacteria adhered to L30 and L50 patterns. In the polished zirconia (Fig. S4.**1a**), quite big and close-packed bacteria agglomeration were observed, while smaller size and more separated bacteria agglomerations were adhered to the microgrooves of the L30 pattern (Fig. S4.**1b**). Interestingly, for L50 pattern (Fig. S4.**1c**), that is composed of more separated microgrooves, we did not observe a striped distribution of the *S. aureus*, suggesting that the bacteria adhere equally to the flat part and grooves. On the contrary, there are less bacteria in both the flat part and the ridges when compared to the control, since the bacteria agglomerations are again smaller and more separated. Finally, *S. aureus* surface coverage on the L100 pattern is similar to one of the polished 3Y-TZP (Fig. S4.**1d**).
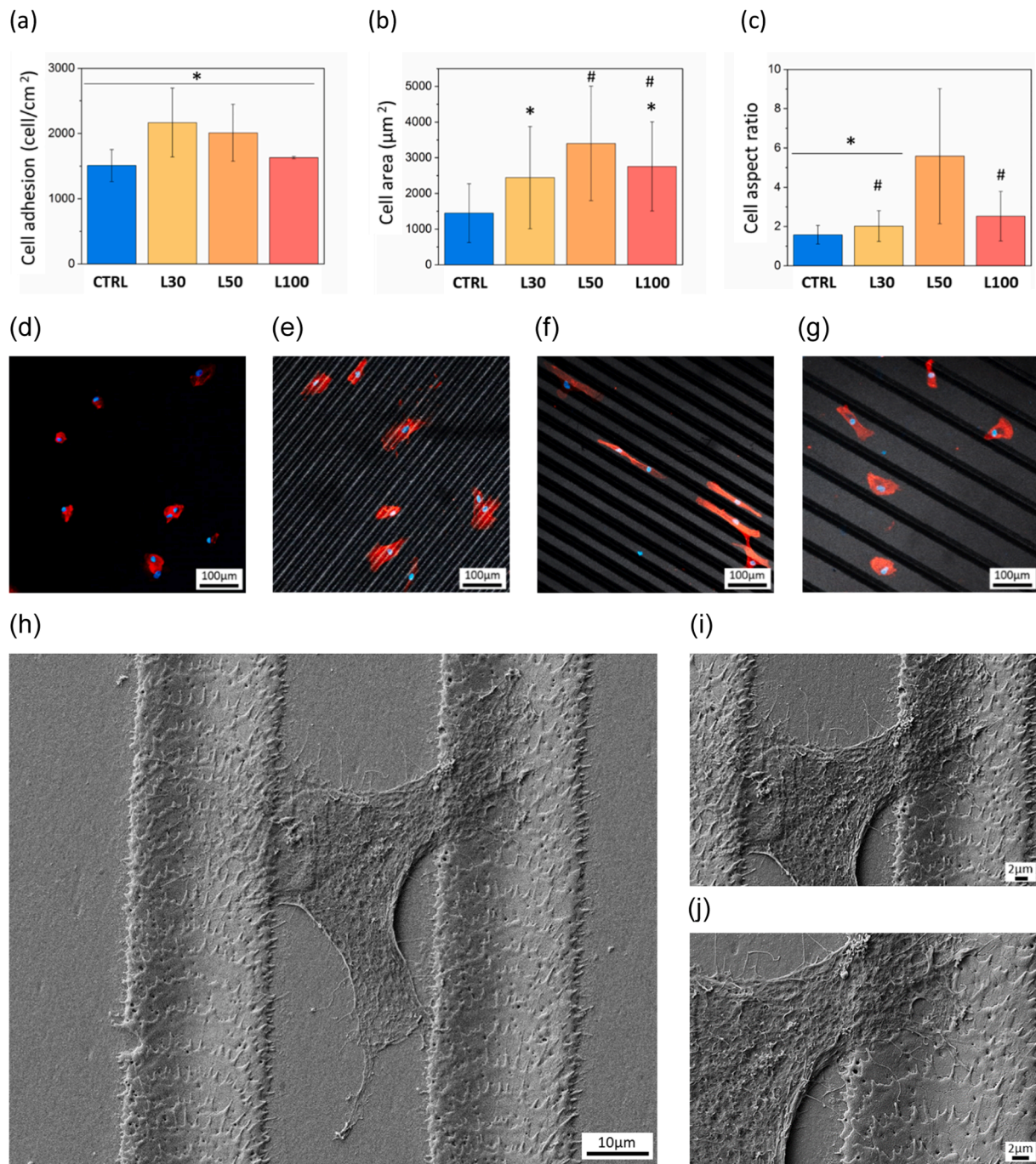
Fig. 5. hMSCs adhesion test results after 6 h of incubation in serum free medium. (a) Cellular adhesion (cell/cm^2), (b) cell area (μm^2), and (c) cell aspect ratio. In the graphs, there are no significative differences among the groups with the same symbol (* or #) ($p < 0.05$). (d)-(g) Representative fluorescence images on the hMSCs cultures on (d) CTRL, (e) L30, (f) L50 and (g) L100 specimen. Actin filaments were stained with Alexa Fluor 488-conjugated phalloidin (red), and cell nuclei with DAPI (blue). (h)FESEM micrographs of a hMSC cultured on the L50 sample. (i)-(j) Magnifications showing the cell anchoring to the laser grooves. The remaining samples are available as supplementary material.

4. Discussion

Laser patterning is a powerful approach to develop cell instructive and antibacterial surfaces for implant applications. In this study, three microgroove patterns of different periodicity (30, 50 and 100 μm) were fabricated on 3Y-TZP by a ns-laser, in order to study the interaction between the cells and the structured surfaces. Furthermore, the effect of laser processing on the topography, microstructure and hydrothermal degradation resistance was also evaluated.

The ns-laser employed allowed the fabrication of well-defined and reproducible groove structures on 3Y-TZP. The pattern formation involved melting and resolidification of the surface material, as evidenced from the melting tracks, pile-up structures, and interconnected crack network generated over the treated surfaces (Fig. 2). This is related to the photothermal material removal mechanism governing in ns- regime [71–73]. In this regime, the pulse duration is longer than the thermalization time of 3Y-TZP, and therefore there is enough time to transfer the heat from the electrons to the surface, leading to a rapid localized heating and melting of the material [74]. Consequently, a temperature gradient is generated on the surface, driving the melted
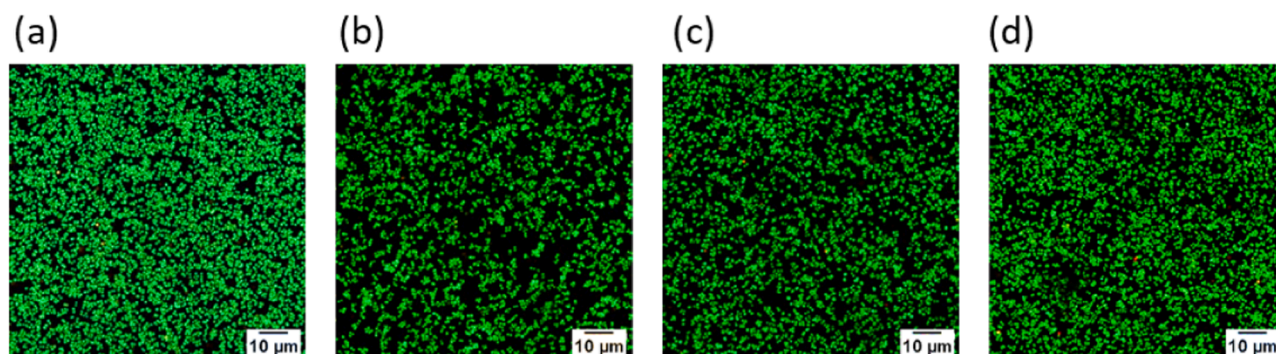
Fig. 6. Fluorescence microscopy images of the live/dead staining of S. aureus after 4 h of incubation. (a) CTRL, (b) L30, (c) L50 and (d) L100. On the images all bacteria are stained in green and dead bacteria in red.

Table 3
Percentage of bacterial adhesion compared to the untreated (CTRL) 3Y-TZP. * Indicated significative different with respect to the CTRL ($p < 0.05$).

S. Aureus adhesion compared to polished zirconia (%)			
CTRL	L30	L50	L100
100	77.5 ± 7.98 *	82.2 ± 0.50 *	89.3 ± 4.83

material to flow from the highest temperature zone to the cold untreated part, where it is then piled and recrystallized [75]. In fact, such a topographical alteration has already been described in the literature on ns-laser treated zirconia. For instance, Roitero *et al.* observed traces of molten material together with interconnected intragranular cracks along the microgroove topography [50,76]. Similarly, Pereira *et al.* reported a "melted like-topography" that presented a scratched morphology because of the thermal cracks produced during the melting and recrystallization [52]. In addition, other surface defects similar to the ones observed in our work, such as the presence of pores, cavities, bumps, asperities, or debris, have been reported [73,77].

The already described topographical damage can be critical for the mechanical reliability of the material [21]. On this respect, femtosecond (fs-) lasers are a great alternative over ns-ones to minimize the surface damage, particularly because the main material removal process is changed from melting to ablation [74]. In the fs- regime, the pulse duration is below the electron-phonon relaxation time so that there is not enough time for the heat transfer and the material is removed mainly by evaporative ablation [31]. Thus, the thermal effect is almost eliminated, and the resulting topography is free of melting tracks and pile-up, and the generated cracks and pores are reduced from micrometric to nanometric size [31,57,78,79].

The damage induced during laser micromachining is not only limited to the surface. The microstructure of 3Y-TZP can also be altered by the exposure to high temperatures and the introduction of thermal stresses that occurred during the laser irradiation [76]. What is more, when working in the ns-regime, a surface layer composed of *m*- grains is expected from the recrystallization of the melted material. In fact, Jing *et al.* [73] measured large *m*- phase volumes by XRD on ns-laser treated 3Y-TZP, which ranged between 50% and 64% (depending on the processing parameters) [73]. The authors attributed this significant phase transformation to the microcracks and high thermal stresses generated during the laser treatment [73]. To a lesser extent, Roitero *et al.* [76] also found approximately 8% of V_m on microgrooved 3Y-TZP produced by a ns-laser, although in that work the surfaces apparently displayed less cracks and lower pile-up. Nevertheless, our microstructural findings differ much from those results. According to the XRD investigation, the *t*-phase was preserved after the laser structuring in the three micro-topographies (Fig. 3b). These results indicated that after melting, the material may have recrystallized again into the *t*- form and not into the

m- one, which may be attributed to a rapid cooling process.

Furthermore, it is crucial to assess the LTD resistance of laser-treated 3Y-TZP when considering its clinical use for dental application. Even though no microstructural changes were observed after the laser surface modification, the introduced surface damage (i.e. microcracks and pits) decreased the hydrothermal degradation resistance of the L30 and L50 patterns when compared to polished zirconia (Fig. 3b). This is because the surface flaws acted as nucleation points for the *t*→*m* transformation during the initial steps of aging [63,66,80]. These results are in agreement with other works using ns-laser [64] and even fs-laser [31,52], in which the reduction in the LTD resistance was associated to the formation of topographical defects (e.g. microcracks), but also to the pre-existing *m*-phase grains at the surface and the internal tensile stresses induced by the thermal shock.

Interestingly, the reduction in LTD resistance seems to be inversely proportional to pattern periodicity, as the L100 condition showed the best aging behavior (V_m 27.07%). This may be explained by the non-homogeneous *m*- phase volume distribution observed on the pattern's surface, after aging, by Raman Spectroscopy analysis (Fig. 4): the V_m was much higher on the laser grooves (the pile-up zone) than on the un-treated zone, as this is the region concentrating more damage due to the presence of microcracks and recrystallized material accumulation. Therefore, as the periodicity between the lines is increased, lower grooves (and therefore lower amount of damage) are included in the XRD analysis spot, and consequently the overall *m*- phase volume of the evaluated spot is lower.

The characteristics of the surface topography plays a significant role on the cell-surface interaction [81]. Laser patterning offers greater control over topography when compared to other methods (i.e. grinding, sandblasting), since it allows the structuring and scalability of different geometrical features. On this respect, several works evidenced that laser patterned topographies improved cell commitment ([53–55, 82–87]), however, it is not clear yet how the dimensions of the structures affect the cell behavior.

On this work, preliminary biological studies were performed to evaluate the effect of laser patterning and microgroove periodicity (30, 50 and 100 μm) on the early response of MSCs, in term of cell adhesion and morphology. Overall, the three microgroove patterns mainly affected cell-shape and spreading, without significant changes in the cell number. The results evidenced that the three laser patterns improved hMSCs response by increasing the area of the adhered cells, meaning that the topographical structures formed on the laser grooves provide the cells more contact points that strengthen cell spreading. Accordingly, increased cell area was also evidenced on other works where microgrooves [31], micropillars [54] and micropits [57] were structured on 3Y-TZP. Additionally, the nascent FAs observed on the three laser patterns confirmed that the cells are capable of stablishing more and stronger cell-surface interactions due to the presence of micro/-nanofeatures [88,89]. In a previous work, Carvalho *et al.* [90] evidenced

mature FAs on fs-laser microgrooved zirconia, and the clustering of the integrins was also associated to the presence of laser induced nano-topography. Of note, it is well known that FAs play a vital role in MSC signaling, and therefore, are essential for various cellular processes such as proliferation, differentiation, and migration [91,92].

Surface topography-modulated MSC morphology was mainly achieved on the L50 specimen. The MSCs adhered to this pattern adopted a very elongated morphology and were aligned according to the groove direction. Furthermore, we observed that many of the elongated cells did not fit inside the grooves, but instead they appeared to be adhered to the non-treated surface. Such preferential position of the hMSCs could be related to the width of the non-treated zone, which is about 25 μm in the L50 sample, very close to the size of hMSCs. The width of the laser groove is also similar, nevertheless, it is composed by the pile-up and the laser valley. Therefore, it seems that the cells do not fit well inside of it, but instead, they use the nanotopography of the grooves to stablish strong cell-surface interactions, as evidenced by the filopodia extending to the lateral grooves (Fig. 5i-j) and the presence of nascent FAs (Fig. S2). This agrees with other studies suggesting that patterns with features close to the cell size can better module the cell response compared with lower or larger size structures [28,93]. Additionally, these microgrooved-like topography mediated changes in the cell morphology and alignment have been well described in the literature [31,54,55,83,94]. In previous studies, such an elongated cell morphology and alignment, coupled with the microgrooves that provides directionality cues to the cells, have been proved to improve MSC migration [31,55]. Also, other studies have pointed out that topographies similar to the microstructures of our work increased bone mineralization and osteogenic related gene expression [83,84]. Nevertheless, neither MSC migration nor differentiation were evaluated in this study.

Any topographical change on the surfaces that enhances eukaryotic cell adhesion may also have an effect in the capacity of bacteria to colonize the surface [20,36,95]. In order to guarantee the survival of the implant it is crucial that the bacteria adhesion is minimum, since otherwise, it can lead to an inflammatory process called peri-implantitis [96]. This can be achieved by fabricating bactericidal or antifouling surfaces [20,97]. As a matter of fact, killing of bacteria by topographical features has only been described for nanostructured surfaces displaying high aspect ratio topographies, e.g. nanoneedles or nanospikes, that impose deformational stresses to bacterial membranes, thus piercing and rupturing them [20]. Such types of high aspect ratio features were absent in our samples.

In our case, even though any bactericidal effect was achieved, the patterns engraved on 3Y-TZP slightly reduced *S. aureus* early adhesion when compared to the polished surface (Table 3). The greatest decrease was observed on the L30 pattern, followed by the L50 one. On this respect, changes in bacterial behavior have often been related to the topography. As concluded in a review by Hasan and Chatterjee, topographies with sub-micro or nanoscale features, which are smaller to the bacterial cell size, may effectively minimize bacterial attachment [96]. In line with this, Helbig *et al.* [95] also proposed a dependence of the initial bacterial retention with the structural dimensions of the surface. Topographies with features greater or in the range of the bacterial size–mostly > 1–2 μm, depending on the bacterial strain – increase the cell-surface contact area, generally leading to higher bacterial settlement. On the contrary, such contact area is decreased on a sub-cell sized topography, where the bacteria can not establish strong bonding with the surface and the early bacterial attachment is restrained. Accordingly, we initially hypothesized that the sub-micrometric size structures/roughness of the grooves, which are below the *S. aureus* size, may inhibit bacterial adhesion (i.e. antifouling effect). Nevertheless, SEM images from the bacterial adhesion assay revealed that bacteria adhere equally to both the flat part and the grooves of the patterns, suggesting that the antifouling effect observed for L30 and L50 conditions is not provided by the topography of the grooves. Thus, with the results obtained from the bacterial assays we cannot make a clear statement on the

underlying anti-bacterial mechanism, but we propose that it could be related to other surface properties, such as changes in the surface energy [98]. Further studies, out of the scope of the present paper, should be directed to elucidate that.

To the best of our knowledge, bacterial adhesion to laser treated 3Y-TZP has not been systematically studied yet. There are only few works in which antibacterial surfaces have been created by laser modification on other materials, mostly titanium and stainless steel [51,99–102]. Such topographies consist on cone-, hole- or ripple-like structures of a size ranging from about 200–800 nm, which showed an antiadhesive effect against different bacterial strains. Nevertheless, in all those studies the patterns were fabricated employing fs-lasers, since achieving such nanometric features with a ns-laser is challenging.

This study provides a general overview of the effects of ns-laser surface modification on the topography, microstructure, hydrothermal degradation resistance and early biological response of 3Y-TZP. We have demonstrated that ns-laser is a suitable approach to produce well-defined and repeatable microgroove structures on 3Y-TZP, while introducing only minor changes in the hydrothermal degradation resistance. Furthermore, it provides new information for understanding the impact of the laser induced topographical features on cell adhesion and, to the best of our knowledge, is one of the pioneers evaluating the bacterial response to laser patterned zirconia. In fact, we were able to improve cell spreading and tune MSC morphology and alignment on the 50-μm microgroove pattern, while slightly decreasing *S. aureus* adhesion at short incubation times. Nonetheless, we acknowledge that these biological studies are preliminary, and that further evaluating the influence of the patterns on MSC differentiation and migration is needed. Additionally, a more comprehensive bacterial characterization should be conducted to elucidate the long-term impact of the patterns on bacterial response and to gain insights into the underlying mechanisms contributing to the observed antibacterial effects.

5. Conclusion

The surface of 3Y-TZP has been modified using a ns-laser and three microgroove patterns have been produced by varying the periodicity (30, 50 and 100 μm). The changes produced in the topography, microstructure, hydrothermal degradation resistance and biological response have been investigated, leading to the following conclusions:

- Surface damage (microcracks and pits) was produced in the three patterns, independently of the periodicity. Other topographical alterations (melting tracks and material pile-up) were also generated.
- The melting tracks and microcracks provided the grooves with additional submicrometer size topography.
- The introduced flaws slightly worsen the LTD resistance of the laser treated 3Y-TZP; however, the decrease was not very significant.
- MSCs adhesion and spreading was improved on the three microgroove patterns.
- The best results in terms of MSC morphology (elongated shape) and alignment were obtained on the 50 μm pattern (L50).
- *S. aureus* adhesion was reduced on 30 μm (L30) and 50 μm (L50) microgroove patterns. The homogeneous distribution of the bacteria along the L50 surface suggested that the reduction may not be due to the topography.

In conclusion, the laser surface modification of 3Y-TZP holds great promise for the design of antibacterial and cell instructive topographies in biomedical applications. In this regard, the use of fs-laser may offer a greater potential for such a purpose, as it enables to gain a better control over the nanoscale topography.

Declaration of Competing Interest

The authors declare that they have no known competing financial

interests or personal relationships that could have appeared to influence the work reported in this paper.

Acknowledgements

Appendix A. Supporting information

Supplementary data associated with this article can be found in the online version at doi:10.1016/j.dental.2023.10.026.

References

[1] Comino-Garayoa R, Brinkmann JCB, Peláez J, López-Suárez C, Martínez-González JM, Suárez MJ. Allergies to titanium dental implants: What do we really know about them? A scoping review. Biol (Basel) 2020;9:1–15. https://doi.org/10.3390/biology9110404.

[2] Fretwurst T, Nelson K, Tarnow DP, Wang HL, Giannobile WV. Is metal particle release associated with peri-implant bone destruction? An emerging concept. J Dent Res 2018;97:259–65. https://doi.org/10.1177/0022034517740560.

[3] Müller K, Valentine-Thon E. Hypersensitivity to titanium: clinical and laboratory evidence. Neuroendocrinol Lett 2006;27:31–5.

[4] Pitta J, Zarauz C, Pjetursson B, Sailer I, Liu X, Pradies G. A systematic review and meta-analysis of the influence of abutment material on peri-implant soft tissue color measured using spectrophotometry. Int J Prosthodont 2020;33:39–47. https://doi.org/10.11607/ijp.6393.

[5] Sala L, Bascones-Martínez A, Carrillo-de-Albornoz A. Impact of abutment material on peri-implant soft tissue color. An in vitro study. Clin Oral Invest 2016;21:2221–33. https://doi.org/10.1007/s00784-016-2015-9.

[6] Piconi C, Maccauro G, Sekar M, Piconi C, Maccauro G. Zirconia as a biomaterial. Biomaterials 1999;20:1–25. https://doi.org/10.1016/B978-0-12-803581-8.10245-0.

[7] Manicone PF, Rossi Iommetti P, Raffaelli L. An overview of zirconia ceramics: basic properties and clinical applications. J Dent 2007;35:819–26. https://doi.org/10.1016/j.jdent.2007.07.008.

[8] Denry I, Kelly JR. State of the art of zirconia for dental applications. Dent Mater 2008;24:299–307. https://doi.org/10.1016/j.dental.2007.05.007.

[9] Covacci V, Bruzzese N, Maccauro G, Andreassi C, Ricci GA, Piconi C, et al. In vitro evaluation of the mutagenic and carcinogenic power of high purity zirconia ceramic. Biomaterials 1999;20:371–6. https://doi.org/10.1016/S0142-9612(98)00182-3.

[10] Degidi M, Artese L, Scarano A, Perrotti V, Gehrke P, Piattelli A. Inflammatory infiltrate, microvessel density, nitric oxide synthase expression, vascular endothelial growth factor expression, and proliferative activity in peri-implant soft tissues around titanium and zirconium oxide healing caps. J Periodo 2006;77:73–80. https://doi.org/10.1902/jop.2006.77.1.73.

[11] Rimondini L, Cerroni L, Carrassi A, Torricelli P. Bacterial colonization of zirconia ceramic surfaces: an in vitro and in vivo study. He Int J Oral Maxillofac Implants 2002;17:793–800.

[12] Roehling S, Astasov-Frauenhoffer M, Hauser-Gerspach I, Braissant O, Woelfler H, Waltimo T, et al. In vitro biofilm formation on titanium and zirconia implant surfaces. J Periodo 2017;88:298–307. https://doi.org/10.1902/jop.2016.160245.

[13] Scarano A, Piattelli M, Caputi S, Favero GA, Piattelli A. Bacterial adhesion on commercially pure titanium and zirconium oxide disks: an in vivo human study. J Periodo 2004;75:292–6. https://doi.org/10.1902/jop.2004.75.2.292.

[14] Clever K, Schlegel KA, Kniha H, Conrads G, Rink L, Modabber A, et al. Experimental peri-implant mucositis around titanium and zirconia implants in comparison to a natural tooth: part 1—host-derived immunological parameters. Int J Oral Maxillofac Surg 2019;48:554–9. https://doi.org/10.1016/j.ijom.2018.10.018.

[15] Wróbel E, Witkowska-Zimny M, Przybylski J. Biological mechanism of implant osseointegration. Ortop Trauma Rehabil 2011;12:401–9.

[16] Roehling S, Schlegel KA, Woelfler H, Gahlert M. Performance and outcome of zirconia dental implants in clinical studies: a meta-analysis. Clin Oral Implants Res 2018;29:135–53. https://doi.org/10.1111/clr.13352.

[17] Hashim D, Cionca N, Courvoisier DS, Mombelli A. A systematic review of the clinical survival of zirconia implants. Clin Oral Invest 2016;20:1403–17. https://doi.org/10.1007/s00784-016-1853-9.

[18] Kohal RJ, Dennison DK. Clinical longevity of zirconia implants with the focus on biomechanical and biological outcome. Curr Oral Health Rep 2020;7:344–51. https://doi.org/10.1007/s40496-020-00289-9.

[19] Mas-Moruno C, Su B, Dalby MJ. Multifunctional coatings and nanotopographies: toward cell instructive and antibacterial implants. Adv Health Mater 2019;8. https://doi.org/10.1002/adhm.201801103.

[20] Mas-Moruno C, Su B, Dalby MJ. Multifunctional coatings and nanotopographies: toward cell instructive and antibacterial implants. Adv Health Mater 2019;8. https://doi.org/10.1002/adhm.201801103.

[21] García-de-Albeniz N, Jiménez-Piqué E, Roa JJ, Mas-Moruno C. A review of surface topographical modification strategies of 3Y-TZP: Effect in the physicochemical properties, microstructure, mechanical reliability, and biological response. J Eur Ceram Soc 2023;43:2977–3004. https://doi.org/10.1016/j.jeurceramsoc.2023.02.043.

[22] Pešáková V, Kubies D, Hulejová H, Himmlová L. The influence of implant surface properties on cell adhesion and proliferation. J Mater Sci Mater Med 2007;18:465–73. https://doi.org/10.1007/s10856-007-2006-0.

[23] Xue T, Attarilar S, Liu S, Liu J, Song X, Li L, et al. Surface modification techniques of titanium and its alloys to functionally optimize their biomedical properties: Thematic review. Front Bioeng Biotechnol 2020;8. https://doi.org/10.3389/FBIOE.2020.603072/BIBTEX.

[24] Liu X, Lim JY, Donahue HJ, Dhurjati R, Mastro AM, Vogler EA. Influence of substratum surface chemistry/energy and topography on the human fetal osteoblastic cell line hFOB 1.19: phenotypic and genotypic responses observed in vitro. Biomaterials 2007;28:4535–50. https://doi.org/10.1016/j.biomaterials.2007.06.016.

[25] Hou Y, Xie W, Yu L, Camacho LC, Nie C, Zhang M, et al. Surface roughness gradients reveal topography-specific mechanosensitive responses in human mesenchymal stem cells. Small 2020;16. https://doi.org/10.1002/smll.201905422.

[26] Long EG, Buluk M, Gallagher MB, Schneider JM, Brown JL. Human mesenchymal stem cell morphology, migration, and differentiation on micro and nano-textured titanium. Bioact Mater 2019;4:249–55. https://doi.org/10.1016/j.bioactmat.2019.08.001.

[27] Albrektsson T, Wennerberg A. Oral implant surfaces: part 1–review focusing on topographic and chemical properties of different surfaces and in vivo responses to them. Int J Prosthodont 2004;17:536–43.

[28] Zhao C, Xia L, Zhai D, Zhang N, Liu J, Fang B, et al. Designing the ordered micropatterned hydroxyapatite bioceramics to promote the growth and osteogenic differentiation of bone marrow stromal cells. J Mater Chem 2015. https://doi.org/10.1039/b000000x.

[29] Carvalho A, Pelaez-Vargas A, Hansford DJ, Fernandes MH, Monteiro FJ. Effects of line and pillar array microengineered SiO2 thin films on the osteogenic differentiation of human bone marrow-derived mesenchymal stem cells. Langmuir 2016;32:1091–100. https://doi.org/10.1021/acs.langmuir.5b03955.

[30] Jeon HJ, Simon CG, Kim GH. A mini-review: cell response to microscale, nanoscale, and hierarchical patterning of surface structure. J Biomed Mater Res B Appl Biomater 2014;102:1580–94. https://doi.org/10.1002/jbm.b.33158.

[31] Minguela J, Müller DW, Mücklich F, Llanes L, Ginebra MP, Roa JJ, et al. Peptidic biofunctionalization of laser patterned dental zirconia: a biochemical-topographical approach. Mater Sci Eng 2021;125. https://doi.org/10.1016/j.msec.2021.112096.

[32] Vasilevich AS, Vermeulen S, Kamphuis M, Roumans N, Eroumé S, Hebels DGAJ, et al. On the correlation between material-induced cell shape and phenotypical response of human mesenchymal stem cells. Sci Rep 2020;10. https://doi.org/10.1038/s41598-020-76019-z.

[33] Subbiahdoss G, Kuijer R, Grijpma DW, van der Mei HC, Busscher HJ. Microbial biofilm growth vs. tissue integration: "The race for the surface" experimentally studied. Acta Biomater 2009;5:1399–404. https://doi.org/10.1016/j.actbio.2008.12.011.

[34] Damiati L, Eales MG, Nobbs AH, Su B, Tsimbouri PM, Salmeron-Sanchez M, et al. Impact of surface topography and coating on osteogenesis and bacterial attachment on titanium implants. J Tissue Eng 2018;9. https://doi.org/10.1177/2041731418790694.

[35] Wu S, Zhang B, Liu Y, Suo X, Li H. Influence of surface topography on bacterial adhesion: a review. Biointerphases 2018;13. https://doi.org/10.1116/1.5054057.

[36] Whitehead KA, Verran J. The effect of surface topography on the retention of microorganisms. Food Bioprod Process 2006;84:253–9. https://doi.org/10.1205/fbp06035.

[37] Yeo I-S, Kim H-Y, Lim KS, Han J-S. Implant surface factors and bacterial adhesion. Int J Artif Organs 2012;35:762–72. https://doi.org/10.5301/ijao.5000154.

[38] Minguela J, Slawik S, Mücklich F, Ginebra MP, Llanes L, Mas-Moruno C, et al. Evolution of microstructure and residual stresses in gradually ground/polished 3Y-TZP. J Eur Ceram Soc 2020;40:1582–91. https://doi.org/10.1016/j.jeurceramsoc.2019.10.057.

[39] Pereira GKR, Fraga S, Montagner AF, Soares FZM, Kleverlaan CJ, Valandro LF. The effect of grinding on the mechanical behavior of Y-TZP ceramics: a systematic review and meta-analyses. J Mech Behav Biomed Mater 2016;63:417–42. https://doi.org/10.1016/j.jmbbm.2016.06.028.

[40] Muñoz-Tabares JA, Jiménez-Piqué E, Reyes-Gasga J, Anglada M. Microstructural changes in ground 3Y-TZP and their effect on mechanical properties. Acta Mater 2011;59:6670–83. https://doi.org/10.1016/j.actamat.2011.07.024.

[41] Chintapalli RK, Mestra Rodriguez A, Garcia Marro F, Anglada M. Effect of sandblasting and residual stress on strength of zirconia for restorative dentistry

applications. J Mech Behav Biomed Mater 2014;29:126–37. https://doi.org/10.1016/j.jmbbm.2013.09.004.

[42] Caravaca CF, Flamant Q, Anglada M, Gremillard L, Chevalier J. Impact of sandblasting on the mechanical properties and aging resistance of alumina and zirconia based ceramics. J Eur Ceram Soc 2018;38:915–25. https://doi.org/10.1016/j.jeurceramsoc.2017.10.050.

[43] Finger C, Stiesch M, Eisenburger M, Breidenstein B, Busemann S, Greuling A. Effect of sandblasting on the surface roughness and residual stress of 3Y-TZP (zirconia). SN Appl Sci 2020;2. https://doi.org/10.1007/s42452-020-03492-6.

[44] Stanciuc AM, Flamant Q, Biotteau-Deheuvels K, Stoddart MJ, Anglada M, Porporati AA, et al. Human primary osteoblast behaviour on microrough zirconia-toughened alumina and on selectively etched microrough zirconia-toughened alumina. J Eur Ceram Soc 2018;38:927–37. https://doi.org/10.1016/j.jeurceramsoc.2017.06.022.

[45] Depprich R, Ommerborn M, Zipprich H, Naujoks C, Handschel J, Wiesmann HP, et al. Behavior of osteoblastic cells cultured on titanium and structured zirconia surfaces. Head Face Med 2008;4(1):9. https://doi.org/10.1186/1746-160X-4-29.

[46] Flamant Q, García Marro F, Roa Rovira JJ, Anglada M. Hydrofluoric acid etching of dental zirconia. Part 1: etching mechanism and surface characterization. J Eur Ceram Soc 2015;36:121–34. https://doi.org/10.1016/j.jeurceramsoc.2015.09.021.

[47] Giner L, Mercadé M, Torrent S, Punset M, Pérez RA, Delgado LM, et al. Double acid etching treatment of dental implants for enhanced biological properties. J Appl Biomater Funct Mater 2018;16:83–9. https://doi.org/10.5301/jabfm.5000376.

[48] Delgado-Ruíz RA, Calvo-Guirado JL, Moreno P, Guardia J, Gomez-Moreno G, Mate-Sánchez JE, et al. Femtosecond laser microstructuring of zirconia dental implants (B) J Biomed Mater Res B Appl Biomater 2011;96:91–100. https://doi.org/10.1002/jbm.b.31743.

[49] Parry JP, Shephard JD, Hand DP, Moorhouse C, Jones N, Weston N. Laser micromachining of zirconia (Y-TZP) ceramics in the picosecond regime and the impact on material strength. Int J Appl Ceram Technol 2011;8:163–71. https://doi.org/10.1111/j.1744-7402.2009.02420.x.

[50] Roitero E, Lasserre F, Anglada M, Mücklich F, Jiménez-Piqué E. A parametric study of laser interference surface patterning of dental zirconia: effects of laser parameters on topography and surface quality. Dent Mater 2017;33:28–38. https://doi.org/10.1016/j.dental.2016.09.040.

[51] Luo X, Yao S, Zhang H, Cai M, Liu W, Pan R, et al. Biocompatible nano-ripples structured surfaces induced by femtosecond laser to rebel bacterial colonization and biofilm formation. Opt Laser Technol 2020;124:105973. https://doi.org/10.1016/j.optlastec.2019.105973.

[52] Pereira RSF, Moura CG, Henriques B, Chevalier J, Silva FS, Fredel MC. Influence of laser texturing on surface features, mechanical properties and low-temperature degradation behavior of 3Y-TZP. Ceram Int 2020;46:3502–12. https://doi.org/10.1016/j.ceramint.2019.10.065.

[53] Ackerl N, Bork AH, Hauert R, Müller E, Rottmar M. Rationally designed ultra-short pulsed laser patterning of zirconia-based ceramics tailored for the bone-implant interface. Appl Surf Sci 2021;545:149020. https://doi.org/10.1016/j.apsusc.2021.149020.

[54] Ferreira BF, da Cruz MB, Marques JF, Madeira S, Carvalho Ó, Silva FS, et al. Laser Nd:YAG patterning enhance human osteoblast behavior on zirconia implants. Lasers Med Sci 2020;35:329–48. https://doi.org/10.1007/s10103-020-03066-3.

[55] Carvalho A, Cangueiro L, Oliveira V, Vilar R, Fernandes MH, Monteiro FJ. Femtosecond laser microstructured Alumina toughened Zirconia: a new strategy to improve osteogenic differentiation of hMSCs. Appl Surf Sci 2018;435:1237–45. https://doi.org/10.1016/j.apsusc.2017.11.206.

[56] Carvalho A, Grenho L, Fernandes MH, Daskalova A, Trifonov A, Buchvarov I, et al. Femtosecond laser microstructuring of alumina toughened zirconia for surface functionalization of dental implants. Ceram Int 2020;46:1383–9. https://doi.org/10.1016/j.ceramint.2019.09.101.

[57] Stanciuc AM, Flamant Q, Sprecher CM, Alini M, Anglada M, Peroglio M. Femtosecond laser multi-patterning of zirconia for screening of cell-surface interactions. J Eur Ceram Soc 2018;38:939–48. https://doi.org/10.1016/j.jeurceramsoc.2017.08.019.

[58] Goyos-Ball L, Prado C, Díaz R, Fernández E, Ismailov A, Kumpulainen T, et al. The effects of laser patterning 10CeTZP-Al2O3 nanocomposite disc surfaces: Osseous differentiation and cellular arrangement in vitro. Ceram Int 2018;44:9472–8. https://doi.org/10.1016/j.ceramint.2018.02.164.

[59] Faria D, Madeira S, Buciumeanu M, Silva FS, Carvalho O. Novel laser textured surface designs for improved zirconia implants performance. Mater Sci Eng C 2020;108. https://doi.org/10.1016/j.msec.2019.110390.

[60] Parry JP, Shephard JD, Dear FC, Jones N, Weston N, Hand DP. Nanosecond-laser postprocessing of millisecond- laser-machined zirconia (Y-TZP) surfaces. Int J Appl Ceram Technol 2008;5:249–57. https://doi.org/10.1111/j.1744-7402.2008.02222.x.

[61] Chevalier J. What future for zirconia as a biomaterial? Biomaterials 2006;27:535–43. https://doi.org/10.1016/j.biomaterials.2005.07.034.

[62] Chevalier J, Gremillard L, Deville S. Low-temperature degradation of zirconia and implications for biomedical implants. Annu Rev Mater Res 2007;37:1–32. https://doi.org/10.1146/annurev.matsci.37.052506.084250.

[63] Muñoz-Tabares JA, Jiménez-Piqué E, Anglada M. Subsurface evaluation of hydrothermal degradation of zirconia. Acta Mater 2011;59:473–84. https://doi.org/10.1016/j.actamat.2010.09.047.

[64] Roitero E, Ochoa M, Anglada M, Mücklich F, Jiménez-Piqué E. Low temperature degradation of laser patterned 3Y-TZP: enhancement of resistance after thermal

treatment. J Eur Ceram Soc 2018;38:1742–9. https://doi.org/10.1016/j.jeurceramsoc.2017.10.044.

[65] Camposilvan E, Flamant Q, Anglada M. Surface roughened zirconia: towards hydrothermal stability. J Mech Behav Biomed Mater 2015;47:95–106. https://doi.org/10.1016/j.jmbbm.2015.03.017.

[66] Chevalier J, Gremillard L, Virkar AV, Clarke DR. The tetragonal-monoclinic transformation in zirconia: lessons learned and future trends. J Am Ceram Soc 2009;92:1901–20. https://doi.org/10.1111/j.1551-2916.2009.03278.x.

[67] Toraya H, Yoshimura M, Somiya S. Calibration curve for quantitative analysis of the monoclinic-tetragonal ZrO2 system by X-ray diffraction. J Am Ceram Soc 1984;67:119–21. https://doi.org/10.1111/j.1151-2916.1984.tb19715.x.

[68] Katagiri G, Ishida H, Ishitani A, Masaki T. Direct determination by a Raman microprobe of the transformation zone size in Y₂O₃ containing tetragonal ZrO₂ polycrystals. Adv Ceram 1986;24:537–44.

[69] Humphreys H. Staphylococcus aureus: the enduring pathogen in surgery. Surgeon 2012;10:357–60. https://doi.org/10.1016/j.surge.2012.05.003.

[70] Minkiewicz-Zochniak A, Jarzynka S, Iwańska A, Strom K, Iwańczyk B, Bartel M, et al. Biofilm formation on dental implant biomaterials by Staphylococcus aureus strains isolated from patients with cystic fibrosis. Materials 2021;14. https://doi.org/10.3390/ma14082030.

[71] Fornaini C, Poli F, Merigo E, Lutey A, Cucinotta A, Chevalier M, et al. Nanosecond pulsed fiber laser irradiation for enhanced zirconia crown adhesion: Morphological, chemical, thermal and mechanical analysis. J Photochem Photobio B 2021;219:112189. https://doi.org/10.1016/j.jphotobiol.2021.112189.

[72] Li J, Ji L, Hu Y, Bao Y. Precise micromachining of yttria-tetragonal zirconia polycrystal ceramic using 532 nm nanosecond laser. Ceram Int 2016;42:4377–85. https://doi.org/10.1016/j.ceramint.2015.11.118.

[73] Jing X, Pu Z, Zheng S, Wang F, Qi H. Nanosecond laser induced microstructure features and effects thereof on the wettability in zirconia. Ceram Int 2020;46:24173–82. https://doi.org/10.1016/j.ceramint.2020.06.197.

[74] Hamad AH. Effects of different laser pulse regimes (nanosecond, picosecond and femtosecond) on the ablation of materials for production of nanoparticles in liquid solution. High Energy Short Pulse Lasers 2016. https://doi.org/10.5772/63892.

[75] Karbalaei A, Kumar R, Cho HJ. Thermocapillarity in microfluidics - a review. Micro (Basel) 2016;7:1–41. https://doi.org/10.3390/mi7010013.

[76] Roitero E, Lasserre F, Roa JJ, Anglada M, Mücklich F, Jiménez-Piqué E. Nanosecond-laser patterning of 3Y-TZP: damage and microstructural changes. J Eur Ceram Soc 2017;37:4876–87. https://doi.org/10.1016/j.jeurceramsoc.2017.05.052.

[77] Hirota M, Harai T, Ishibashi S, Mizutani M, Hayakawa T. Cortical bone response toward nanosecond-pulsed laser-treated zirconia implant surfaces. Dent Mater J 2019;38:444–51. https://doi.org/10.4012/dmj.2018-153.

[78] Yamamuro Y, Shimoyama T, Yamashita I, Yan J. Microscale surface patterning of zirconia by femtosecond pulsed laser irradiation. Int J Precis Eng Manuf-Green Technol 2021. https://doi.org/10.1115/1.4046040.

[79] Zhou H, Li C, Zhou Z, Cao R, Chen Y, Zhang S, et al. Femtosecond laser-induced periodic surface microstructure on dental zirconia ceramic. Mater Lett 2018;229:74–7. https://doi.org/10.1016/j.matlet.2018.06.059.

[80] Lughi V, Sergo V. Low temperature degradation -aging- of zirconia: a critical review of the relevant aspects in dentistry. Dent Mater 2010;26:807–20. https://doi.org/10.1016/j.dental.2010.04.006.

[81] Wennerberg A, Albrektsson T. On implant surfaces: a review of current knowledge and opinions. Int J Oral Maxillofac Implants 2010;25:63–74.

[82] Minguela Díaz J. Surface Characterization And Cell Instructive Properties Of Superficially Modified Dental Zirconia. Universitat Politècnica de Catalunya; 2021.

[83] Delgado-Ruíz RA, Gomez Moreno G, Aguilar-Salvatierra A, Markovic A, Mate-Sánchez JE, Calvo-Guirado JL. Human fetal osteoblast behavior on zirconia dental implants and zirconia disks with microstructured surfaces. An experimental in vitro study. Clin Oral Implants Res 2015;00:1–10. https://doi.org/10.1111/clr.12585.

[84] Rezaei NM, Hasegawa M, Ishijima M, Nakhaei K, Okubo T, Taniyama T, et al. Biological and osseointegration capabilities of hierarchically (meso-/micro-/nano-scale) roughened zirconia. Int J Od Nanomed 2018;13:3381–95.

[85] Lee BEJ, Exir H, Weck A, Grandfield K. Characterization and evaluation of femtosecond laser-induced sub-micron periodic structures generated on titanium to improve osseointegration of implants. Appl Surf Sci 2018;441:1034–42. https://doi.org/10.1016/j.apsusc.2018.02.119.

[86] Klos A, Sedao X, Itina T, Helfenstein-Didier C, Donnet C, Peyroche S, et al. Ultrafast laser processing of nanostructured patterns for the control of cell adhesion and migration on titanium alloy. Nanomaterials 2020;10. https://doi.org/10.1109/cleo/europe-eqec52157.2021.9541931.

[87] Daskalova A, Angelova L, Carvalho A, Trifonov A, Nathala C, Monteiro F, et al. Effect of surface modification by femtosecond laser on zirconia based ceramics for screening of cell-surface interaction. Appl Surf Sci 2020;513:1–15. https://doi.org/10.1016/j.apsusc.2020.145914.

[88] Lim JY, Dreiss AD, Zhou Z, Hansen JC, Siedlecki CA, Hengstebeck RW, et al. The regulation of integrin-mediated osteoblast focal adhesion and focal adhesion kinase expression by nanoscale topography. Biomaterials 2007;28:1787–97. https://doi.org/10.1016/j.biomaterials.2006.12.020.

[89] Luo J., Walker M., Xiao Y., Donnelly H., Dalby M.J., Salmeron-Sanchez M. The influence of nanotopography on cell behaviour through interactions with the extracellular matrix-A review 2021. https://doi.org/10.1016/j.bioactmat.2021.11.024.

[90] Carvalho A, Cangueiro L, Oliveira V, Vilar R, Fernandes MH, Monteiro FJ. Femtosecond laser microstructured Alumina toughened Zirconia: a new strategy to improve osteogenic differentiation of hMSCs. Appl Surf Sci 2018;435:1237–45. https://doi.org/10.1016/j.apsusc.2017.11.206.

[91] Yamaguchi N., Knaut H. Focal adhesion-mediated cell anchoring and migration: from in vitro to in vivo 2022. https://doi.org/10.1242/dev.200647.

[92] Zhao Y, Sun Q, Huo B, Yz Bh, Yz, et al. Focal adhesion regulates osteogenic differentiation of mesenchymal stem cells and osteoblasts. Biomater Transl 2021; 2:312–22. https://doi.org/10.12336/biomatertransl.2021.04.007.

[93] Zhao G, Schwartz Z, Wieland M, Rupp F, Geis-Gerstorfer J, Cochran DL, et al. High surface energy enhances cell response to titanium substrate microstructure. J Biomed Mater Res A 2005;74:49–58. https://doi.org/10.1002/jbm.a.30320.

[94] Dumas V, Rattner A, Vico L, Audouard E, Dumas JC, Naisson P, et al. Multiscale grooved titanium processed with femtosecond laser influences mesenchymal stem cell morphology, adhesion, and matrix organization (A) J Biomed Mater Res A 2012;100:3108–16. https://doi.org/10.1002/jbm.a.34239.

[95] Helbig R, Günther D, Friedrichs J, Rößler F, Lasagni A, Werner C. The impact of structure dimensions on initial bacterial adhesion. Biomater Sci 2016;4:1074–8. https://doi.org/10.1039/c6bm00078a.

[96] Hasan J, Chatterjee K. Recent advances in engineering topography mediated antibacterial surfaces. Nanoscale 2015;7:15568–75. https://doi.org/10.1039/c5nr04156b.

[97] Zheng, Bawazir S, Dhall M, Kim HE A, He L, Heo J, et al. Implication of surface properties, bacterial motility, and hydrodynamic conditions on bacterial surface sensing and their initial adhesion. Front Bioeng Biotechnol 2021;9:1–22. https://doi.org/10.3389/fbioe.2021.643722.

[98] Zheng, Bawazir S, Dhall M, Kim HE A, He L, Heo J, et al. Implication of surface properties, bacterial motility, and hydrodynamic conditions on bacterial surface sensing and their initial adhesion. Front Bioeng Biotechnol 2021;9:1–22. https://doi.org/10.3389/fbioe.2021.643722.

[99] Lutey AHA, Gemini L, Romoli L, Lazzini G, Fuso F, Faucon M, et al. Towards laser-textured antibacterial surfaces. Sci Rep 2018;8:1–10. https://doi.org/10.1038/s41598-018-28454-2.

[100] Cunha A, Elie AM, Plawinski L, Serro AP, Botelho Do Rego AM, Almeida A, et al. Femtosecond laser surface texturing of titanium as a method to reduce the adhesion of Staphylococcus aureus and biofilm formation. Appl Surf Sci 2016; 360:485–93. https://doi.org/10.1016/j.apsusc.2015.10.102.

[101] Peter A, Lutey AHA, Faas S, Romoli L, Onuseit V, Graf T. Direct laser interference patterning of stainless steel by ultrashort pulses for antibacterial surfaces. Opt Laser Technol 2020;123. https://doi.org/10.1016/j.optlastec.2019.105954.

[102] Epperlein N, Menzel F, Schwibbert K, Koter R, Bonse J, Sameith J, et al. Influence of femtosecond laser produced nanostructures on biofilm growth on steel. Appl Surf Sci 2017;418:420–4. https://doi.org/10.1016/j.apsusc.2017.02.174.